ACS Catalysis

pubs.acs.org/acscatalysis Research Article

Unconventional High-Index Facet of Iridium Boosts Oxygen Evolution Reaction: How the Facet Matters

Fei Xue,[‖] Xinyang Guo,[‖] Boya Min, Yitao Si, Hongwen Huang, Jinwen Shi, and Maochang Liu*

Cite This: ACS Catal. 2021, 11, 8239−8246 Read Online

ACCESS | Metrics & More | Article Recommendations | Supporting Information

ABSTRACT: Iridium (Ir) nanostructures with well-defined shapes, and particularly, highly active surface, are attractive for the application of electrocatalytic oxygen evolution reaction (OER), yet they have had very limited success to date because of challenges in their synthesis. Here, we report the synthesis of Ir nanocrystals, in the form of Pd@Ir core−shell structures and with well-defined high-index {331} facets, by a robust seed-mediated process. The success relies on the precise control over the deposition of ultrathin Ir layer on Pd trioctahedral nanocrystals. The Pd@Ir nanocatalyst with such unique high-index facets delivers substantially promoted OER activity and durability compared with those with low-index facets (i.e., {100} and {111} facets), with an overpotential as low as 300 mV, boosted mass activities up to 1.01 A mg_{Ir}^{-1} at 1.53 V, and a minimal Tafel slope of 84.9 mV dec^{-1}. Density functional theory (DFT) calculations suggest that the superior OER performance originates from the easier hydroxylation of *O to *OOH over high-index facets, along with the appropriate value of ΔG_O-ΔG_{OH} and satisfactory adsorption/desorption property. Moreover, the high-index facets are apt to be electrochemically oxidized into stable IrO_x species, leading to an improved durability. Both theoretical and experimental studies demonstrate the fascinating property of a high-index Ir shell in facilitating OER activity and durability.

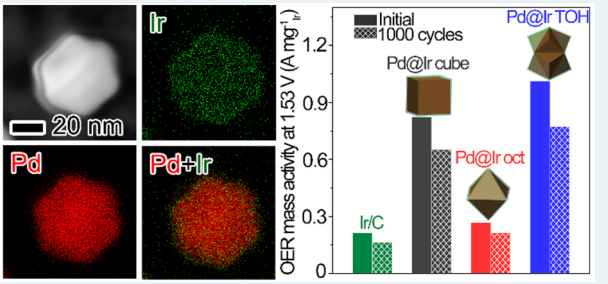

KEYWORDS: *iridium, trioctahedron, high-index facet, core−shell nanostructure, oxygen evolution reaction*

INTRODUCTION

Water splitting is currently deemed as a feasible technology to achieve scalable conversion from surplus electric-power toward clean hydrogen energy.[1−4] Nevertheless, the oxygen evolution reaction (OER), as involving multiple-electron steps, is usually constrained by the intrinsically sluggish kinetics, bringing about a high-energy demand to create O═O bonds.[1−7] Even worse, the serious leaching and dissolution of electrocatalysts in acidic/alkaline media upon long-term operation largely hampers its large-scale commercialization.[8−10] Thus, the development of an OER electrocatalyst with cost efficiency, high activity, and excellent corrosion-resistance is highly anticipated. Derived from its balance of activity and durability, Ir is perceived as a state-of-the-art electrocatalyst candidate for OER, especially in the acidic condition.[5,9−18]

However, considering the extremely low reserves, continual consumption, as well as high cost of Ir, the maximum utilization of Ir atoms should be imperatively guaranteed.[14,18,19] To this end, the composition, size, morphology, and structure of Ir-based catalysts have all been manipulated to intensify the electrocatalytic performance.[5,10,14−18,20−24] Thereinto, one of the most viable approaches is constructing Ir-based core−shell nanostructure via seed-mediated growth, with Ir atoms in several atomic layers as an ultrathin shell and more abundant and/or cheap materials as interior cores.[14,18,25−27] However, because of the lower energy barrier for homogeneous nucleation than that for heterogeneous nucleation, Ir atoms usually prefer to the island growth instead of epitaxial deposition on substrates.[26,28] This inherent attribute makes it extremely hard to investigate the facet-dependent catalytic properties for the Ir single crystal. Thankfully, Xia's group has recently achieved growth habit alteration of Ir at the atomic level via kinetic control over diffusion/deposition rates of Ir atoms.[14,25−30] In this way, a series of Pd@Ir core−shell nanostructures with cubic and octahedral morphologies and thus surface-dependent catalytic properties were acquired.[14,18,25−27] Yet, the success was primarily targeted on low-index exposed surface (i.e. {100} for nanocube and {111} for nanoctahedron) with low specific surface free energy. High-index facets generally can manifest higher catalytic activity when benchmarked against their low-index counterparts because of the abundance of low-coordinated surface atoms at atomic steps, edges, and

Received: April 24, 2021
Revised: June 4, 2021

https://doi.org/10.1021/acscatal.1c01867
ACS Catal. 2021, 11, 8239−8246

kinks,[31−34] while further progress is limited by the synthesis. This limitation makes it incomprehensive and shallow to elucidate the relationship between OER performance and surface atomic structures. In this context, engineering of high-index facets in atomic accuracy for the Ir surface and conducting a comparative study on their OER behavior remain unmet but significant challenges.

Herein, we demonstrate the facet-controlled construction of Pd@Ir core−shell nanostructures via conformal deposition of Ir shell on Pd seeds with various shapes (e.g., cubes (cube), octahedron (oct), and trioctahedron (TOH)). With ultrathin Ir shells in atomic dimension, Pd@Ir cube, Pd@Ir oct, and Pd@Ir TOH displayed well-defined Ir {100}, {111}, and {331} facets, respectively. Both density functional theory (DFT) calculations and electrochemical measurements cooperatively verified a facet-dependent catalytic behavior of these Pd@Ir core−shell nanostructures toward OER. Thereinto, Pd@Ir TOH with high-index facets experimentally delivered maximal activity and durability, with an overpotential (η) of 300 mV at 10 mA cm_{geo}^{-2} and a mass activity of 1.01 A mg_{Ir}^{-1} at η = 300 mV. Meanwhile, the DFT calculation analysis provides a nearly quantitative agreement with the experimental data. Thus, synthesis of high-index facets can serve as a new entry point for design of highly active OER catalysts.

RESULTS AND DISCUSSION

A classical two-step strategy, involving preparation of monodispersed Pd seeds and subsequently seed-mediated growth, was employed in our synthesis. As shown in Figure S1 and S2, the morphologies of the as-prepared seeds for the following overgrowth of Ir are indexed into the well-defined Pd cube, octahedron, and trioctahedron, with average edge lengths of 45.33 ± 4.07, 50.02 ± 3.82, and 49.23 ± 3.36 nm, respectively. Notably, these three Pd seeds were all uniform in both shape and size. On the basis of HRTEM images, the polyhedral projective profile, and the relationship between projection angle and Miller indices of facets (Figure S1 and Table S1), the surfaces of Pd cubic, octahedral, and trioctahedral seeds were dominatingly enclosed by {100}, {111}, and high-indexed {331}, respectively. Subsequently, Pd@Ir cube, Pd@Ir oct, and Pd@Ir TOH were successfully constructed via kinetic control over the deposition rate ($V_{dep.}$) and diffusion rate ($V_{diff.}$) of Ir adatoms. It is known that a larger atom diffusion rate, compared with deposition rate ($V_{diff.} > V_{dep.}$), can ensure the conformal, layer-by-layer deposition of Ir adatoms on surfaces of Pd seeds (Figure 1a).[10,26−30,35,36] Under this circumstance, a low injection rate (thus small $V_{dep.}$) of Ir precursor and an elevated reaction temperature (thus large $V_{diff.}$) were applied in this seed-mediated growth. It is necessary to emphasize that in order to reduce the surface energy for high-index surface, the Ir adatoms on surface of Pd trioctahedral seeds tend to spontaneously diffuse all over the surface area, and thus, a lower temperature input (in this case, 130 °C) is sufficient to achieve the criteria of $V_{diff.} > V_{dep.}$. Figure 1b−d depict the TEM images of as-synthesized Pd@Ir cube, Pd@Ir oct, and Pd@Ir TOH with satisfactory size and morphology homogeneity, demonstrating the well-maintained Pd seeds during the overgrowth of Ir atoms. A more intuitive observation by scanning electron microscope (SEM) testified the morphological inheritance of nanocube, nanoctahedron, and nanotrioctahedron for Pd@Ir core−shell nanocrystals from Pd seeds (Figure S3). Meanwhile, a close examination of flat and smooth surfaces in Pd@Ir core−shell configurations

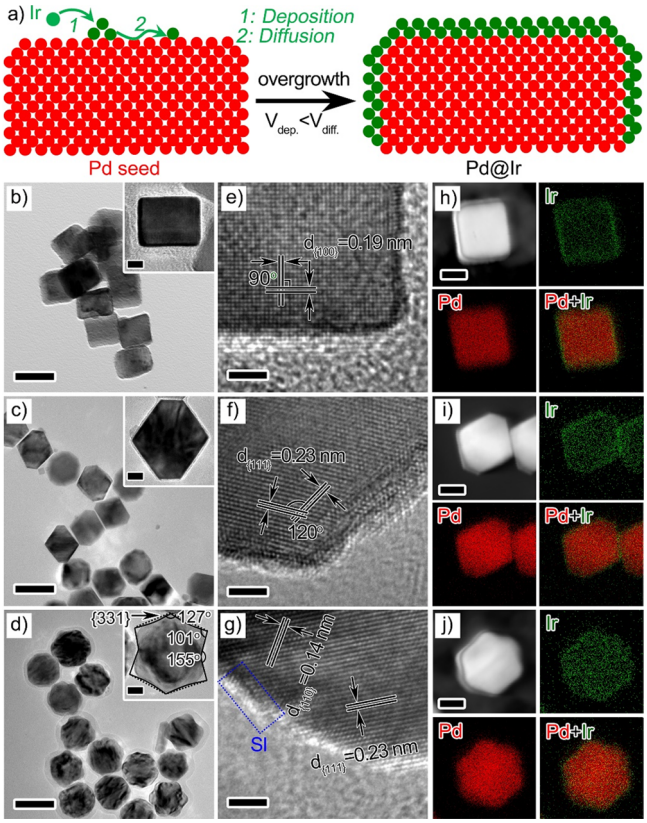

Figure 1. (a) Schematic illustration of the Pd seed-mediated Ir growth. (b−d) TEM images of Pd@Ir cube, Pd@Ir oct, and Pd@Ir TOH, respectively (scale bar: 50 nm). The insets in these three figures show the individual nanoparticles in high magnification, respectively (scale bar: 10 nm). (e−g) HRTEM image of Pd@Ir cube, Pd@Ir oct, and Pd@Ir TOH, respectively (scale bar: 2 nm). The blue dashed box in panel g marks the area that requires a closer investigation in Figure S4a. (h−j) HAADF-STEM images of Pd@Ir cube, Pd@Ir oct, and Pd@Ir TOH and corresponding energy-dispersive X-ray spectroscopy mapping of Pd and Ir (scale bar: 20 nm).

(insets in Figure 1b−d) implies that the Ir growth indeed follows the layer-by-layer mode. More importantly, the high-resolution TEM (HRTEM) images (Figure 1e−g) recorded from individual Pd@Ir core−shell nanocrystals certified continuous lattice fringes from Pd core to Ir shell. These results demonstrated the epitaxial growth of Ir shells from their respective Pd cores. In other words, the three Pd@Ir core−shell nanostructures were terminated by {100}, {111}, and {331} facets of a face-centered cubic (fcc) Ir, respectively, as indexed from well-resolved lattice spacing,[14,25−27,37] together with the projection angle and atomic arrangement models projected from the [1$\bar{1}$0] direction (Figure 1e−g, Table S1, and Figure S4).[38] To be more explicit, the combination of a one-atom-wide (111) and two-atom-wide (110) (Figure S4), designated as 1(111) × 2(110) according to microfacet notation theory, constitutes the high-index (331) facet.

In addition, the statistical results of size distribution illustrate increased average edge lengths of 45.74 ± 4.13 nm, 50.51 ± 3.45 nm and 49.41 ± 2.61 nm for Pd@-Ir cube, Pd@-Ir oct, and Pd@-Ir TOH, respectively, relative to those of Pd nanocrystals (Figure S5). As a result, the thicknesses of Ir shell on Pd cubic, octahedral, and trioctahedral seeds could be estimated to be about 0.21, 0.24, and 0.09 nm, respectively.

https://doi.org/10.1021/acscatal.1c01867
ACS Catal. 2021, 11, 8239−8246

Consequently, a one-atomic-layer thickness of the Ir shell for these three samples can be speculated according to corresponding Ir interplanar distances. The average numbers (n) of Ir atomic layers in Pd@Ir core−shell nanostructures were further analyzed by inductively coupled plasma mass spectrometry (ICP-MS). As summarized in Tables S2 and S3, the values of n in Pd@Ir cube, Pd@Ir oct, and Pd@Ir TOH were determined to be 0.8, 0.8, and 1.0, respectively, again indicating ultrathin monolayer coatings of the Ir shell on all Pd seeds. In the meantime, the consistency of the typical single nanocrystals in different projected profiles (highlighted in red dashed circle in Figure S5c, labeled 1−3) with the three-dimensional (3D) TOH models observed along <111>, <110>, and <100> directions (Figure S6) further certifies the successful formation of Pd@Ir TOH nanostructures. Subsequently, the scanning TEM (STEM) and corresponding energy-dispersive X-ray spectroscopy (EDX) mapping (Figure 1h−j) intuitively verified the conformal deposition of the ultrathin Ir shell on the surfaces of Pd seeds. The EDX line-scanning profiles across individual Pd@Ir cube, Pd@Ir oct, and Pd@Ir TOH nanocrystals, as shown in Figure S7a−c, provide direct proof of the elemental configuration involving Ir shells and Pd cores.

The intrinsically crystalline structure of the Pd@Ir core−shell configurations were further identified by X-ray diffraction (XRD), as depicted in Figure 2a. Obviously, all the

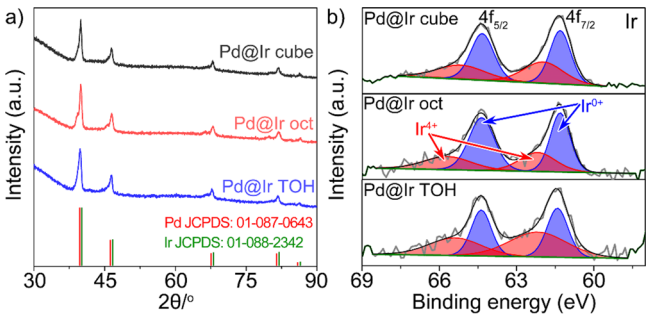

Figure 2. (a) XRD patterns and (b) Ir 4f high-resolution XPS spectra in Pd@Ir cube, Pd@Ir oct, and Pd@Ir TOH.

characteristic peaks indexed to fcc-Pd can be easily detected in these core−shell nanostructures. The characteristic diffractions of Ir shells were imperceptible for all samples that could be attributed to the small loading amount and diffraction peak overlap with those of the Pd cores. With regards to standard diffraction patterns of Pd (JCPDS 01-087-0643) and Ir (JCPDS 01-088-2342), the virtually identical diffraction angles for all samples can be found, implying successful formation of core−shell configurations rather than alloyed forms. Furthermore, the similar full widths at half-maximum for these three samples foreboded comparable nanoparticle sizes according to Scherrer's equation, in good consistency with TEM characterization. Subsequently, the X-ray photoelectron spectroscopy (XPS) was conducted to understand in-depth the surface chemical composition and valence states of these Pd@Ir core−shell nanocrystals. As observed in Figure S8, the doublet peaks located at 335.9 and 341.4 eV, assignable to the Pd^0 $3d_{5/2}$ and $3d_{3/2}$ peaks,[14,18,25,27,30] certified the zero-valence state of the Pd cores. Meanwhile, the absence of oxidation states in Pd indicated the construction of flat and hermetic Ir shell. For the Ir shells (Figure 2b), while two major peaks at 61.3 eV ($4f_{7/2}$) and 64.3 eV ($4f_{5/2}$) could be assigned to metallic Ir, the other two minor ones at higher binding energies (62.1 for $4f_{7/2}$ and 65.5 eV for $4f_{5/2}$) were resulted from Ir^{4+}.[10,12−18,21,24,25] This phenomenon is likely derived from the inevitable surface oxidation of Ir shell upon exposure in atmosphere. More interestingly, quantitative XPS analysis via area integral revealed a gradual increase of the proportion of the oxidized Ir in the composites with a sequence of Pd@Ir TOH > Pd@Ir cube > Pd@Ir oct (Figure S9 and Table S4). In principle, the highest susceptibility to air oxidation for trioctahedral Ir shell should be a result of the high-index characters with atomic unsaturated coordination.[39] It is worth pointing out that the oxidized Ir has been well-accepted as the major active species for OER.[14−16,18,40] For that reason, a considerably high OER catalytic activity for Pd@Ir TOH can be expected. Collectively, the three Pd@Ir core−shell nanostructures with diversified exposed facets of Ir shells—but in the same size, atomic layer, and weight percentage—are thus ideal model catalysts to investigate the electrocatalytic activities toward OER.

Subsequently, to evaluate the facet-dependent catalytic performance, OER tests in $HClO_4$ aqueous solution were implemented via a rotating disk electrode (RDE). The RDE was configured with an Ir loading amount of 9.5 $\mu g_{Ir} \cdot cm^{-2}$ for each of the samples. The OER activity of the Pd@Ir core−shell nanocrystals was benchmarked with that of a commercial Ir/C catalyst (size ∼4.6 nm, see Figure S10). Notably, the Pd@Ir core−shell nanostructures were first homogeneously dispersed on carbon supports (label as Pd@Ir cube/C, Pd@Ir oct/C, and Pd@Ir TOH/C) (Figure S11) and then, together with commercial Ir/C, treated within acetic acid at 60 °C for 3 h to clean the surface before being dropped on RDE. To reveal the Ir shell triggered OER property, the cyclic voltammetry (CV) curves recorded between 0.05 and 1.2 V (vs RHE) of Pd@Ir core−shell catalysts and corresponding Pd seeds were initially performed to detect their oxygenated species affinity.[41,42] Notably, the platinum-group metals, such as Pt, Pd, and Ir, are featured with the significant hydrogen adsorption−desorption peak in CVs (0.05−0.4 V vs RHE), making it hard to distinguish the actual origination of this region.[43,44] Therefore, our concerns shifted to the characteristic reduction peaks for Pd oxides and Ir oxides in back scan. Generally, the reduction of Ir(IV), either already existing in the shell or irreversibly converted from metallic Ir during CV scan (0.8−1.2 V vs RHE), is kinetically impeded.[44−46] Only Ir(III) obtained during positive CV sweeping (0.4−0.8 V vs RHE) from metallic Ir can be reversibly reduced, bringing about a characteristic reduction peak with a different potential from Pd oxides.[44−46] Specifically, as observed in Figure S12a−c, all Pd seeds are featured with a reduction peak at around 0.75 V (vs RHE) that indicates surface oxide.[42,47] By contrast, this reduction peak is indiscernible in CV of Pd@Ir core−shell catalysts. Instead, a distinguished reduction peak located at around 0.65 V (vs RHE) assigned to the electrochemically reversible Ir(III) oxide can be perceptible.[45,48,49] This notion manifested the effective passivation of Ir shell to Pd core.

Prior to the OER activity detection, a stabilizing CV scanning for surface activation is indispensable to all the electrocatalysts. Figure 3a shows the OER polarization curves of the three core−shell configurations and the commercial Ir/C. Clearly, Pd@Ir TOH/C presented the lowest onset potential (∼1.38 V) with regard to Pd@Ir cube/C (∼1.40 V), Pd@Ir oct/C (∼1.42 V), and commercial Ir/C (∼1.43 V), verifying the superiority of the high-index facet toward

https://doi.org/10.1021/acscatal.1c01867
ACS Catal. 2021, 11, 8239−8246

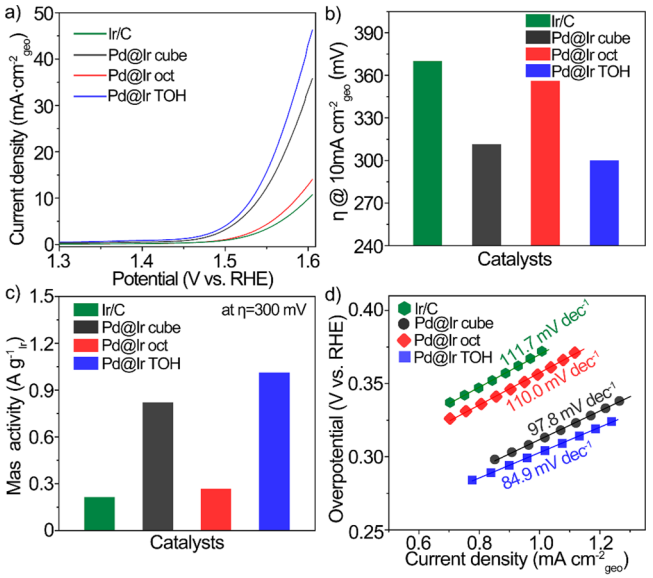

Figure 3. (a) LSV curves at an Ir loading of 9.5 $\mu g_{Ir}\cdot cm^{-2}$ on RDE (vs RHE), (b) η to reach 10 mA·cm_{geo}^{-2}, (c) mass activities at η = 300 mV, and (d) Tafel plots for Ir/C, Pd@Ir cube/C, Pd@Ir oct/C, and Pd@Ir TOH/C catalysts.

triggering OER. Analogously, Pd@Ir TOH/C with a high-index surface required the smallest overpotential (η, 300 mV) in comparison to those for Pd@Ir cubes/C (311.5 mV), Pd@Ir oct/C (356 mV), and commercial Ir/C (370 mV) to reach a current density of 10 mA cm_{geo}^{-2} (Figure 3b). The currents at a referenced overpotential (η = 300 mV) were then normalized by Ir content to acquire the intrinsic mass activities, respectively. As illustrated in Figure 3c, these core−shell catalysts displayed a similar tendency toward OER in term of mass activity, with the maximum values (1.01 A mg_{Ir}^{-1}) obtained over the Pd@Ir TOH/C catalyst, demonstrating the feasibility to control the catalytic activity via introducing high-index facets. Notably, the mass activities of Pd@Ir TOH/C, Pd@Ir cubes/C, and Pd@Ir oct/C were about 4.7-, 3.8-, and 1.2-fold relative to that of commercial Ir/C, respectively. It should be noted that the possible ligand and/or strain effects arising from the Pd core underlying the Ir surface should make contribution to the concomitant enhancement of OER activity, akin to the other bimetallic core−shell nanocrystals.[14,28,30,35,50] However, the different improvements in OER activity for Pd@Ir TOH, Pd@Ir cube, and Pd@Ir oct imply the facet-dependent ligand and/or strain effects.[50,51] Particularly, such effects would be amplified over the high-index surface as a result of the introduction of atomic steps and kinks with low coordination numbers in high densities. Additionally, the corresponding Tafel plots were investigated to get more insight into their OER kinetics (Figure 3d and Figure S13). The Tafel slopes of Pd@Ir cube/C, Pd@Ir oct/C, Pd@Ir TOH/C, and Ir/C were estimated to be 97.8, 110.0, 84.9, and 111.7 mV dec^{-1}, respectively, certifying much faster OER kinetics for core−shell catalysts, as well as the facet-dependent OER kinetics of these various catalysts. The lowest Tafel slope gained over Pd@TOH/C catalyst again demonstrates the superiority of the high-index facet in accelerating the reaction. As a result, Pd@TOH/C exhibited a much higher per-site turnover frequency (TOF, 0.49 s^{-1}) than those over Pd@Ir cube/C (0.39 s^{-1}), Pd@Ir oct/C (0.13 s^{-1}), and commercial Ir/C (0.11 s^{-1}) catalysts, as shown in Figure S14. These results explicitly elucidate the critical role of the coordination environment of surface Ir atoms on their intrinsic activity.

To acquire a deep insight into the surface structure-dependent OER performance, DFT computations were conducted on the basis of a four-step proton-coupled electron-transfer pathway (H_2O → *OH → *O → *OOH → O_2).[5,12,20,21,24] It is particularly important to take into account the preadsorption of oxygen atoms on Ir facets.[24] After screening the possible active sites on the three facets, the most favorable chemisorption configurations of intermediates are depicted in Figure S15 and Figure 4a. These results unraveled

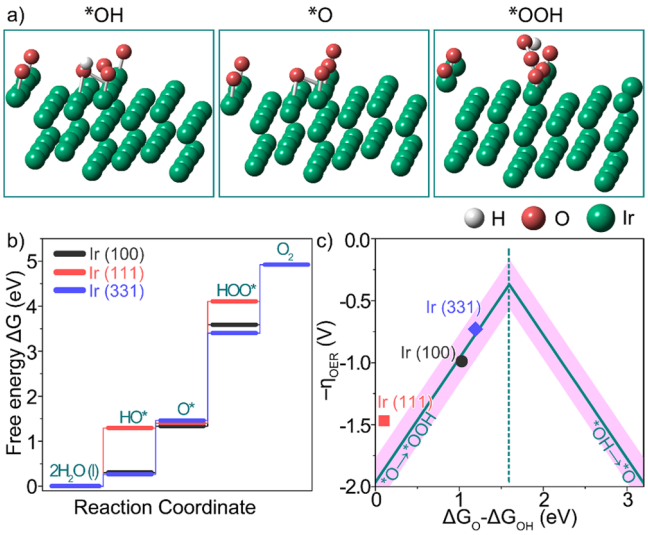

Figure 4. (a) Chemisorption models of intermediates on Ir (331) facet in acidic condition. Keynote: green balls = Ir atoms, red balls = O atoms, and white balls = H atoms, respectively. (b) Free energy diagram for OER on Ir (100), Ir (111), and Ir (331) facets at U = 0 V. (c) The calculated overpotential (η) against the standard free energy of ΔG_O-ΔG_{HO} on Ir (100), Ir (111), and Ir (331) facets.

the great impacts for surface atomic arrangement to the bonding of the surface-oxygenated intermediates. According to Figure 4b, Figure S16, and Tables S5−S7, *OOH species generation from *O was identified to be the potential-determining step (PDS) for all these evaluated facets due to the highest uphill energy barriers (ΔG_3) involved.[20,24] Clearly, the lowest ΔG_3 was achieved over the Ir (331) facet, which was only 1.96 eV in comparison to those of Ir (100) (2.22 eV) and Ir (111) (2.70 eV) facets. This understanding manifested a greater feasibility for high-index facets to overcome the overpotential and thus the PDS to realize an outstanding OER behavior. It is worth pointing out that compared with the experimental values, higher overpotentials were observed over all these facets. This increment may stem from the simplified models that were employed.[24,52] Nevertheless, their variation tendency is identical. Furthermore, the deprotonation of adsorbed H_2O molecules to form *OH intermediates laboriously occurred on Ir (111) facet as it possesses the highest ΔG_1 (1.23 eV) with regard to that of Ir (100) facet (0.30 eV) and Ir (331) facet (0.26 eV). This stumble would result in a backward initial reaction step over Ir (111) facet (Figure S16 and Tables S5−S7). Moreover, the free energy diagrams from DFT calculation can be used to qualitatively reflect reaction kinetics.[53−56] Taken together, these steps synergistically contributed to the highest four-electron OER

https://doi.org/10.1021/acscatal.1c01867
ACS Catal. 2021, 11, 8239−8246

kinetics in acidic medium for high-index facets, in good agreement with our experimental results.

The standard free energy difference ($\Delta G_O - \Delta G_{OH}$) is another widely applied descriptor for evaluating OER performance.[1,12,52,57,58] Generally, by associating theoretical overpotential and $\Delta G_O - \Delta G_{OH}$ based upon universal scaling relations, a volcano-type relationship can be established to seek, predict, and compare the potential OER electrocatalysts (Figure 4c).[53,57,58] Specifically, at the peak region with $\Delta G_O - \Delta G_{OH}$ = 1.6 eV, both the hydroxyl oxidation (*OH → *O) and O−O bond formation (*O → *OOH) are in a properly mild state with the same uphill energy barrier. Meanwhile, the oxygenated intermediates can realize the favorable intermediary adsorption/desorption.[57] In our case, theoretical overpotential and $\Delta G_O - \Delta G_{OH}$ have been well-balanced over the high-index (331) facet of Ir, with the position closest to the top of the volcano. This notion may be a result of the surface-structure-dependent ligand and/or strain effects.[50,51] This notion theoretically explains that why a better OER behavior could be expected over the high-index Ir surface.

As another property metrics, the OER durability of the Pd@Ir cube/C, Pd@Ir oct/C, and Pd@Ir TOH/C catalysts was also evaluated through an accelerated durability test with the commercial Ir/C as a reference. The OER polarization curves for all the samples after 1000-time-cycling tests (1.2−1.6 V vs RHE) were displayed in Figure 5a and Figure S17. Apparently, activity decline occurred on all the samples. Nevertheless, Pd@Ir TOH/C still preserved the best OER activity, as judged from the smallest overpotential at 10 mA·cm$_{geo}^{-2}$ and highest mass activity at 1.53 V (Figure 5a−c and Figure S17). Specifically, after 1000 cycles of test (1.2−1.6 V vs RHE), η at 10 mA·cm$_{geo}^{-2}$ for Pd@Ir TOH/C exhibited a positive shift of 10 mV, whereas amplified variations were observed for Pd@Ir cube/C (11.5 mV), Pd@Ir oct/C (20.7 mV), and Ir/C (20.0 mV). Likewise, at η = 300 mV, Pd@Ir TOH/C still kept ahead in absolute value of mass activity after reversibility test. Quantitatively, the activity losses of 20.7%, 21.0%, and 23.8% were observed for Pd@Ir cube, Pd@Ir oct/C, and Pd@Ir TOH/C, respectively, on par with that for commercial Ir/C (24.2%) (Figure 5c). The comparable decrement in activity indicates a relatively good stability of the high-index surface. The durability of the high-index Ir surface was further validated through Tafel slope variation before and after the long-term test (Figure 5d and Figure S13). Significantly, after 1000 cycles of test (1.2−1.6 V vs RHE), the Tafel slopes of Pd@Ir cube/C and Pd@Ir oct/C were escalated to 109.2 and 121.0 mV dec^{-1}, respectively, while Pd@Ir TOH/C presented nearly identical Tafel slopes. Note that although the variation for commercial Ir/C's Tafel slope is likewise inconspicuous, the largest value implies a sluggish OER kinetics. The OER chronopotentiometry measurement for Pd@Ir core−shell nanocrystals and commercial Ir/C catalysts at current density of 10 mA cm$_{geo}^{-2}$ was also performed (Figure S18). Interestingly, only Pd@Ir TOH/C presented nearly constant potential during a 4-h-test, further demonstrating its prominent stability. Consequently, we can still expect the access to superior OER kinetics from the high-index-facet catalyst even after a long-time operation in the harsh acidic condition.

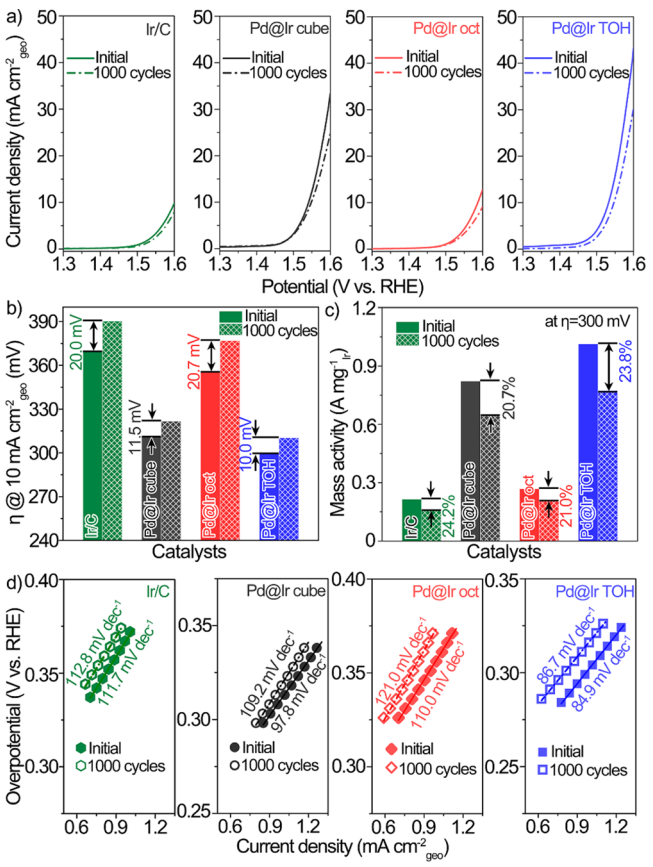

Figure 5. (a) LSV curves, (b) η at 10 mA·cm$_{geo}^{-2}$, (c) mass activities at η = 300 mV, and (d) Tafel plots of Ir/C, Pd@Ir cube/C, Pd@Ir oct/C, and Pd@Ir TOH/C catalysts before and after 1000 cycles of durability test.

To shed more light on the morphological and compositional stability, all Pd@Ir core−shell nanostructures were characterized by TEM, ICP-MS, and XPS after a 1000-cycle test. As displayed in TEM (Figure S19 a−c), although some of the Pd@Ir nanocrystals were found with dissolution-induced structure deterioration, most of the original core−shell structures and morphologies were well-maintained. A closer characterization on the structure-degraded Pd@Ir core−shell nanocrystals revealed the occurrence of surface deformation after 1000 cycling test (Figure S19d−i). However, it is worth pointing out that the basic structure and exposed facet were well-preserved for these mutative core−shell nanocrystals. Significantly, the signal intensities in EDX mappings for both Pd and Ir of all the defective samples have also suffered pronounced decay (Figure S19j−l). The reason could be attributed to the dissolution and degradation of Pd and/or Ir during electrolysis, as intuitively verified by ICP-MS analysis on Ir and Pd ions in the electrolytes after 1000 cycles. Nevertheless, as indicated by Figure S20 and Table S8, all the Ir-based catalysts showed relatively good durability for the reaction with the dissolved ion concentration at ppb level. It is worth pointing out that the dissolution of Pd and Ir would also diminish the ligand and/or strain effects, leading to the slightly declined OER activity. To further understand the activity and mass loss of the Pd@Ir core−shell catalysts, the valence state of Ir and Pd in the core−shell structure was analyzed by XPS spectra. As revealed in Figure S21a, after the initial activation, oxidized forms of IrO_x (i.e., Ir^{4+} and Ir^{y+}, $y > 4$) were induced in both low-index and high-index metallic Ir overlayers.[14−16,18,24] Actually, these oxides have been demonstrated to be the active and stable species in OER for Ir-based catalysts.[14−16,18,40] In principle, the ultrathin atomic-layer

https://doi.org/10.1021/acscatal.1c01867
ACS Catal. 2021, 11, 8239−8246

feature and unsaturated coordination of the high-index facets would lead to an easier and more tendentious electrochemical oxidization of Pd@Ir TOH surface, which is beneficial for harvesting higher OER activity. Meanwhile, it was found that Pd@Ir TOH possessed the largest proportion of Ir^{4+} species in IrO_x (Figure S21a, Figure S22, and Table S9). Generally, Ir^{4+} (e.g., IrO_2) is usually more stable than that of Ir^{y+} during OER.[9,14,18,40] This notion also explains the preferable OER durability of the Pd@Ir TOH catalyst. Note that Pd in Pd@Ir core−shell nanostructures could also be partially oxidized into PdO_x during electrolysis (see Figure S21b). This oxidation should take partial responsibility for the activity and stability decay.[18] Nonetheless, the similar proportion of PdO_x in Pd cores of all the samples can ensure the validity to identify the correlation between structural features and OER activity.

CONCLUSION

In this work, we have demonstrated a conformal disposition of ultrathin Ir shell on Pd TOH seeds with high-index {331} facets. The obtained Pd@Ir TOH with high-index {331} facets delivered the substantially reduced OER overpotential and increased mass activity, as well as smaller Tafel slopes, in comparison to those of the Pd@Ir cube with {100} facets and Pd@Ir oct with {111} facets. Rationalized by DFT calculations, the superior OER behaviors for high-index facets were originated from the lowest uphill energy barrier, moderate $\Delta G_O - \Delta G_{OH}$ value, and compromised binding state with intermediates. In the meantime, the high tendency to electrochemical oxidization on high-index facts led to the formation of a more active and stable surface structure during electrolysis, resulting in a much better OER durability of Pd@Ir TOH. This work offers an accessible strategy for the rational design of core−shell nanostructures with a high-index surface toward efficient and stable electrocatalysis.

ASSOCIATED CONTENT

Supporting Information

The Supporting Information is available free of charge at https://pubs.acs.org/doi/10.1021/acscatal.1c01867.

Experimental details and procedures; Calculation details and corresponding results; Physicochemical characterizations, including SEM, (HR)TEM, EDX line scan, XPS spectra, ICP analysis data of Pd@Ir cube, Pd@Ir oct and Pd@Ir TOH and commercial Ir/C; OER performance test, including CV curves, Tafel slopes, TOF, LSV curves and OER chronopotentiometry measurement of Pd@Ir cube, Pd@Ir oct and Pd@Ir TOH and commercial Ir/C.

(PDF)

AUTHOR INFORMATION

Corresponding Author

Maochang Liu − *International Research Center for Renewable Energy & State Key Laboratory of Multiphase Flow in Power Engineering, Xi'an Jiaotong University, Xi'an, Shaanxi 710049, P. R. China; Suzhou Academy of Xi'an Jiaotong University, Suzhou, Jiangsu 215123, P. R. China;* orcid.org/0000-0002-2371-4060; Phone: +86-(29)-82668296-18; Email: maochangliu@mail.xjtu.edu.cn; Fax: +86-(29)-82669033

Authors

Fei Xue − *International Research Center for Renewable Energy & State Key Laboratory of Multiphase Flow in Power Engineering, Xi'an Jiaotong University, Xi'an, Shaanxi 710049, P. R. China;* orcid.org/0000-0002-7779-4932

Xinyang Guo − *International Research Center for Renewable Energy & State Key Laboratory of Multiphase Flow in Power Engineering, Xi'an Jiaotong University, Xi'an, Shaanxi 710049, P. R. China*

Boya Min − *International Research Center for Renewable Energy & State Key Laboratory of Multiphase Flow in Power Engineering, Xi'an Jiaotong University, Xi'an, Shaanxi 710049, P. R. China*

Yitao Si − *International Research Center for Renewable Energy & State Key Laboratory of Multiphase Flow in Power Engineering, Xi'an Jiaotong University, Xi'an, Shaanxi 710049, P. R. China*

Hongwen Huang − *College of Materials Science and Engineering, Hunan University, Changsha, Hunan 410082, P. R. China;* orcid.org/0000-0003-3967-6182

Jinwen Shi − *International Research Center for Renewable Energy & State Key Laboratory of Multiphase Flow in Power Engineering, Xi'an Jiaotong University, Xi'an, Shaanxi 710049, P. R. China;* orcid.org/0000-0001-7291-2840

Complete contact information is available at: https://pubs.acs.org/10.1021/acscatal.1c01867

Author Contributions

[‖]F.X. and X.G. contributed equally to this manuscript.

Notes

The authors declare no competing financial interest.

ACKNOWLEDGMENTS

This work was supported by the National Nature Science Foundation of China (No. 51888103, No. 51876173), Fok Ying-Tung Education Foundation (No. 171048), the Natural Science Foundation of Jiangsu Province (No. BK20190054), the China Fundamental Research Funds for the Central Universities, and the Shaanxi Technical Innovation Guidance Project (No. 2018HJCG-14).

REFERENCES

(1) Li, L.; Wang, P.; Shao, Q.; Huang, X. Metallic nanostructures with low dimensionality for electrochemical water splitting. *Chem. Soc. Rev.* **2020**, *49*, 3072−3106.

(2) Wu, Z.-P.; Lu, X. F.; Zang, S.-Q.; Lou, X. W. Non-noble-metal-based electrocatalysts toward the oxygen evolution reaction. *Adv. Funct. Mater.* **2020**, *30*, 1910274.

(3) Hong, W. T.; Risch, M.; Stoerzinger, K. A.; Grimaud, A.; Suntivich, J.; Shao-Horn, Y. Toward the rational design of non-precious transition metal oxides for oxygen electrocatalysis. *Energy Environ. Sci.* **2015**, *8*, 1404−1427.

(4) Jiao, S.; Fu, X.; Zhang, L.; Zeng, Y.; Huang, H. Point-defect-optimized electron distribution for enhanced electrocatalysis: Towards the perfection of the imperfections. *Nano Today* **2020**, *31*, 100833.

(5) Shi, Q.; Zhu, C.; Zhong, H.; Su, D.; Li, N.; Engelhard, M. H.; Xia, H.; Zhang, Q.; Feng, S.; Beckman, S. P.; Du, D.; Lin, Y. Nanovoid incorporated Ir_xCu metallic aerogels for oxygen evolution reaction catalysis. *ACS Energy Lett.* **2018**, *3*, 2038−2044.

(6) Suntivich, J.; May, K. J.; Gasteiger, H. A.; Goodenough, J. B.; Shao-Horn, Y. A perovskite oxide optimized for oxygen evolution catalysis from molecular orbital principles. *Science* **2011**, *334*, 1383.

(7) Chen, G.; Zhou, W.; Guan, D.; Sunarso, J.; Zhu, Y.; Hu, X.; Zhang, W.; Shao, Z. Two orders of magnitude enhancement in oxygen evolution reactivity on amorphous $Ba_{0.5}Sr_{0.5}Co_{0.8}Fe_{0.2}O_{3-\delta}$ nanofilms with tunable oxidation state. *Sci. Adv.* **2017**, *3*, e1603206.
(8) Li, X.; Wang, H.; Cui, Z.; Li, Y.; Xin, S.; Zhou, J.; Long, Y.; Jin, C.; Goodenough, J. B. Exceptional oxygen evolution reactivities on $CaCoO_3$ and $SrCoO_3$. *Sci. Adv.* **2019**, *5*, eaav6262.
(9) Pi, Y.; Zhang, N.; Guo, S.; Guo, J.; Huang, X. Ultrathin laminar Ir superstructure as highly efficient oxygen evolution electrocatalyst in broad pH range. *Nano Lett.* **2016**, *16*, 4424−4430.
(10) Zhu, J.-Y.; Xue, Q.; Xue, Y.-Y.; Ding, Y.; Li, F.-M.; Jin, P.; Chen, P.; Chen, Y. Iridium nanotubes as bifunctional electrocatalysts for oxygen evolution and nitrate reduction reactions. *ACS Appl. Mater. Interfaces* **2020**, *12*, 14064−14070.
(11) Antolini, E. Iridium as catalyst and cocatalyst for oxygen evolution/reduction in acidic polymer electrolyte membrane electrolyzers and fuel cells. *ACS Catal.* **2014**, *4*, 1426−1440.
(12) Seitz, L. C.; Dickens, C. F.; Nishio, K.; Hikita, Y.; Montoya, J.; Doyle, A.; Kirk, C.; Vojvodic, A.; Hwang, H. Y.; Nørskov, J. K.; Jaramillo, T. F. A highly active and stable $IrO_x/SrIrO_3$ catalyst for the oxygen evolution reaction. *Science* **2016**, *353*, 1011.
(13) Zhong, W.; Lin, Z.; Feng, S.; Wang, D.; Shen, S.; Zhang, Q.; Gu, L.; Wang, Z.; Fang, B. Improved oxygen evolution activity of IrO_2 by in situ engineering of an ultra-small Ir sphere shell utilizing a pulsed laser. *Nanoscale* **2019**, *11*, 4407−4413.
(14) Zhu, J.; Lyu, Z.; Chen, Z.; Xie, M.; Chi, M.; Jin, W.; Xia, Y. Facile synthesis and characterization of $Pd@Ir_{nL}$ (n = 1−4) core-shell nanocubes for highly efficient oxygen evolution in acidic media. *Chem. Mater.* **2019**, *31*, 5867−5875.
(15) Choi, S.; Park, J.; Kabiraz, M. K.; Hong, Y.; Kwon, T.; Kim, T.; Oh, A.; Baik, H.; Lee, M.; Paek, S.-M.; Choi, S.-I.; Lee, K. Pt dopant: Controlling the Ir oxidation states toward efficient and durable oxygen evolution reaction in acidic media. *Adv. Funct. Mater.* **2020**, *30*, 2003935.
(16) Lv, F.; Zhang, W.; Yang, W.; Feng, J.; Wang, K.; Zhou, J.; Zhou, P.; Guo, S. Ir-based alloy nanoflowers with optimized hydrogen binding energy as bifunctional electrocatalysts for overall water splitting. *Small Methods* **2020**, *4*, 1900129.
(17) Zhu, M.; Shao, Q.; Qian, Y.; Huang, X. Superior overall water splitting electrocatalysis in acidic conditions enabled by bimetallic Ir-Ag nanotubes. *Nano Energy* **2019**, *56*, 330−337.
(18) Zhu, J.; Chen, Z.; Xie, M.; Lyu, Z.; Chi, M.; Mavrikakis, M.; Jin, W.; Xia, Y. Iridium-based cubic nanocages with 1.1-nm-thick walls: A highly efficient and durable electrocatalyst for water oxidation in an acidic medium. *Angew. Chem., Int. Ed.* **2019**, *58*, 7244−7248.
(19) Jiao, S.; Yao, Z.; Li, M.; Mu, C.; Liang, H.; Zeng, Y.; Huang, H. Accelerating oxygen evolution electrocataltsis of two-dimensional NiFe layered double hydroxide nanosheets via space confined amorphization. *Nanoscale* **2019**, *11*, 18894−18899.
(20) Luo, F.; Hu, H.; Zhao, X.; Yang, Z.; Zhang, Q.; Xu, J.; Kaneko, T.; Yoshida, Y.; Zhu, C.; Cai, W. Robust and stable acidic overall water splitting on Ir single atoms. *Nano Lett.* **2020**, *20*, 2120−2128.
(21) Zhao, Y.; Luo, M.; Chu, S.; Peng, M.; Liu, B.; Wu, Q.; Liu, P.; de Groot, F. M. F.; Tan, Y. 3D nanoporous iridium-based alloy microwires for efficient oxygen evolution in acidic media. *Nano Energy* **2019**, *59*, 146−153.
(22) Wu, X.; Feng, B.; Li, W.; Niu, Y.; Yu, Y.; Lu, S.; Zhong, C.; Liu, P.; Tian, Z.; Chen, L.; Hu, W.; Li, C. M. Metal-support interaction boosted electrocatalysis of ultrasmall iridium nanoparticles supported on nitrogen doped graphene for highly efficient water electrolysis in acidic and alkaline media. *Nano Energy* **2019**, *62*, 117−126.
(23) Zhang, T.; Liao, S.-A.; Dai, L.-X.; Yu, J.-W.; Zhu, W.; Zhang, Y.-W. Ir-Pd nanoalloys with enhanced surface-microstructure-sensitive catalytic activity for oxygen evolution reaction in acidic and alkaline media. *Sci. China Mater.* **2018**, *61*, 926−938.
(24) Guo, H.; Fang, Z.; Li, H.; Fernandez, D.; Henkelman, G.; Humphrey, S. M.; Yu, G. Rational design of rhodium-iridium alloy nanoparticles as highly active catalysts for acidic oxygen evolution. *ACS Nano* **2019**, *13*, 13225−13234.
(25) Xi, Z.; Gao, W.; Xia, X. Size effect in Pd-Ir core-shell nanoparticles as nanozymes. *ChemBioChem* **2020**, *21*, 2440−2444.
(26) Xia, X.; Figueroa-Cosme, L.; Tao, J.; Peng, H.-C.; Niu, G.; Zhu, Y.; Xia, Y. Facile synthesis of iridium nanocrystals with well-controlled facets using seed-mediated growth. *J. Am. Chem. Soc.* **2014**, *136*, 10878−10881.
(27) Xia, X.; Zhang, J.; Lu, N.; Kim, M. J.; Ghale, K.; Xu, Y.; McKenzie, E.; Liu, J.; Ye, H. Pd-Ir core-shell nanocubes: A type of highly efficient and versatile peroxidase mimic. *ACS Nano* **2015**, *9*, 9994−10004.
(28) Choi, S.-I.; Young, A.; Lee, S. R.; Ma, C.; Luo, M.; Chi, M.; Tsung, C.-K.; Xia, Y. Pd@Rh core-shell nanocrystals with well-defined facets and their enhanced catalytic performance towards CO oxidation. *Nanoscale Horiz.* **2019**, *4*, 1232−1238.
(29) Xia, X.; Xie, S.; Liu, M.; Peng, H.-C.; Lu, N.; Wang, J.; Kim, M. J.; Xia, Y. On the role of surface diffusion in determining the shape or morphology of noble-metal nanocrystals. *Proc. Natl. Acad. Sci. U. S. A.* **2013**, *110*, 6669.
(30) Xie, S.; Choi, S.-I.; Lu, N.; Roling, L. T.; Herron, J. A.; Zhang, L.; Park, J.; Wang, J.; Kim, M. J.; Xie, Z.; Mavrikakis, M.; Xia, Y. Atomic layer-by-layer deposition of Pt on Pd nanocubes for catalysts with enhanced activity and durability toward oxygen reduction. *Nano Lett.* **2014**, *14*, 3570−3576.
(31) Qian, J.; Shen, M.; Zhou, S.; Lee, C.-T.; Zhao, M.; Lyu, Z.; Hood, Z. D.; Vara, M.; Gilroy, K. D.; Wang, K.; Xia, Y. Synthesis of Pt nanocrystals with different shapes using the same protocol to optimize their catalytic activity toward oxygen reduction. *Mater. Today* **2018**, *21*, 834−844.
(32) Poerwoprajitno, A. R.; Gloag, L.; Cheong, S.; Gooding, J. J.; Tilley, R. D. Synthesis of low- and high-index faceted metal (Pt, Pd, Ru, Ir, Rh) nanoparticles for improved activity and stability in electrocatalysis. *Nanoscale* **2019**, *11*, 18995−19011.
(33) Li, X.; Liu, Y.; Bi, W.; Bi, J.; Guo, R.; Li, R.; Wang, C.; Zhan, Q.; Wang, W.; Yang, S.; Shi, F.; Wu, J.; Jin, M. Lattice-mismatch-induced growth of ultrathin Pt shells with high-index facets for boosting oxygen reduction catalysis. *J. Mater. Chem. A* **2020**, *8*, 16477−16486.
(34) Li, M.; Yuan, Y.; Yao, Z.; Gao, L.; Zhang, J.; Huang, H. Applications of metal nanocrystals with twin defects in electrocatalysis. *Chem. - Asian J.* **2020**, *15*, 3254−3265.
(35) Wang, X.; Choi, S.-I.; Roling, L. T.; Luo, M.; Ma, C.; Zhang, L.; Chi, M.; Liu, J.; Xie, Z.; Herron, J. A.; Mavrikakis, M.; Xia, Y. Palladium-platinum core-shell icosahedra with substantially enhanced activity and durability towards oxygen reduction. *Nat. Commun.* **2015**, *6*, 7594.
(36) Wang, W.; Li, X.; He, T.; Liu, Y.; Jin, M. Engineering surface structure of Pt nanoshells on Pd nanocubes to preferentially expose active surfaces for ORR by manipulating the growth kinetics. *Nano Lett.* **2019**, *19*, 1743−1748.
(37) Li, X.; Li, X.; Liu, C.; Huang, H.; Gao, P.; Ahmad, F.; Luo, L.; Ye, Y.; Geng, Z.; Wang, G.; Si, R.; Ma, C.; Yang, J.; Zeng, J. Atomic-level construction of tensile-strained PdFe alloy surface toward highly efficient oxygen reduction electrocatalysis. *Nano Lett.* **2020**, *20*, 1403−1409.
(38) Yu, Y.; Zhang, Q.; Liu, B.; Lee, J. Y. Synthesis of nanocrystals with variable high-index Pd facets through the controlled heteroepitaxial growth of trisoctahedral Au templates. *J. Am. Chem. Soc.* **2010**, *132*, 18258−18265.
(39) Zhang, W.; Shen, Y.; Pang, F.; Quek, D.; Niu, W.; Wang, W.; Chen, P. Facet-dependent catalytic performance of Au nanocrystals for electrochemical nitrogen reduction. *ACS Appl. Mater. Interfaces* **2020**, *12*, 41613−41619.
(40) Park, J.; Sa, Y. J.; Baik, H.; Kwon, T.; Joo, S. H.; Lee, K. Iridium-based multimetallic nanoframe@nanoframe structure: An efficient and robust electrocatalyst toward oxygen evolution reaction. *ACS Nano* **2017**, *11*, 5500−5509.
(41) Wang, G.; Huang, B.; Xiao, L.; Ren, Z.; Chen, H.; Wang, D.; Abruña, H. D.; Lu, J.; Zhuang, L. Pt skin on AuCu intermetallic

https://doi.org/10.1021/acscatal.1c01867
ACS Catal. 2021, 11, 8239−8246

substrate: A strategy to maximize Pt utilization for fuel cells. *J. Am. Chem. Soc.* **2014**, *136*, 9643−9649.
(42) Li, M.; Luo, M.; Xia, Z.; Yang, Y.; Huang, Y.; Wu, D.; Sun, Y.; Li, C.; Chao, Y.; Yang, W.; Yang, W.; Yu, Y.; Guo, S. Modulating the surface segregation of PdCuRu nanocrystals for enhanced all-pH hydrogen evolution electrocatalysis. *J. Mater. Chem. A* **2019**, *7*, 20151−20157.
(43) Godínez-Salomón, F.; Albiter, L.; Alia, S. M.; Pivovar, B. S.; Camacho-Forero, L. E.; Balbuena, P. B.; Mendoza-Cruz, R.; Arellano-Jimenez, M. J.; Rhodes, C. P. Self-supported hydrous iridium-nickel oxide two-dimensional nanoframes for high activity oxygen evolution electrocatalysts. *ACS Catal.* **2018**, *8*, 10498−10520.
(44) Cherevko, S.; Geiger, S.; Kasian, O.; Mingers, A.; Mayrhofer, K. J. J. Oxygen evolution activity and stability of iridium in acidic media. Part 1. - Metallic iridium. *J. Electroanal. Chem.* **2016**, *773*, 69−78.
(45) Reier, T.; Oezaslan, M.; Strasser, P. Electrocatalytic oxygen evolution reaction (OER) on Ru, Ir, and Pt catalysts: A comparative study of nanoparticles and bulk materials. *ACS Catal.* **2012**, *2*, 1765−1772.
(46) Özer, E.; Spöri, C.; Reier, T.; Strasser, P. Iridium (111), Iridium (110), and Ruthenium (0001) single crystals as model catalysts for the oxygen evolution reaction: Insights into the electrochemical oxide formation and electrocatalytic activity. *ChemCatChem* **2017**, *9*, 597−603.
(47) Liu, S.; Xiao, W.; Wang, J.; Zhu, J.; Wu, Z.; Xin, H.; Wang, D. Ultralow content of Pt on Pd-Co-Cu/C ternary nanoparticles with excellent electrocatalytic activity and durability for the oxygen reduction reaction. *Nano Energy* **2016**, *27*, 475−481.
(48) Yuan, L.; Yan, Z.; Jiang, L.; Wang, E.; Wang, S.; Sun, G. Gold-iridium bifunctional electrocatalyst for oxygen reduction and oxygen evolution reactions. *J. Energy Chem.* **2016**, *25*, 805−810.
(49) Kwon, T.; Hwang, H.; Sa, Y. J.; Park, J.; Baik, H.; Joo, S. H.; Lee, K. Cobalt assisted synthesis of IrCu hollow octahedral nanocages as highly active electrocatalysts toward oxygen evolution reaction. *Adv. Funct. Mater.* **2017**, *27*, 1604688.
(50) Xiong, Y.; Shan, H.; Zhou, Z.; Yan, Y.; Chen, W.; Yang, Y.; Liu, Y.; Tian, H.; Wu, J.; Zhang, H.; Yang, D. Tuning surface structure and strain in Pd-Pt core-shell nanocrystals for enhanced electrocatalytic oxygen reduction. *Small* **2017**, *13*, 1603423.
(51) Carnis, J.; Gao, L.; Fernández, S.; Chahine, G.; Schülli, T. U.; Labat, S.; Hensen, E. J. M.; Thomas, O.; Hofmann, J. P.; Richard, M.-I. Facet-dependent strain determination in electrochemically synthetized platinum model catalytic nanoparticles. *Small* **2021**, *17*, 2007702.
(52) Retuerto, M.; Pascual, L.; Calle-Vallejo, F.; Ferrer, P.; Gianolio, D.; Pereira, A. G.; García, Á.; Torrero, J.; Fernández-Díaz, M. T.; Bencok, P.; Peña, M. A.; Fierro, J. L. G.; Rojas, S. Na-doped ruthenium perovskite electrocatalysts with improved oxygen evolution activity and durability in acidic media. *Nat. Commun.* **2019**, *10*, 2041.
(53) Reier, T.; Nong, H. N.; Teschner, D.; Schlögl, R.; Strasser, P. Electrocatalytic oxygen evolution reaction in acidic environments-reaction mechanisms and catalysts. *Adv. Energy Mater.* **2017**, *7*, 1601275.
(54) Nishimoto, T.; Shinagawa, T.; Naito, T.; Takanabe, K. Microkinetic assessment of electrocatalytic oxygen evolution reaction over iridium oxide in unbuffered conditions. *J. Catal.* **2020**, *391*, 435−445.
(55) Ping, Y.; Nielsen, R. J.; Goddard, W. A., III The reaction mechanism with free energy barriers at constant potentials for the oxygen evolution reaction at the IrO_2 (110) surface. *J. Am. Chem. Soc.* **2017**, *139*, 149−155.
(56) Mavros, M. G.; Tsuchimochi, T.; Kowalczyk, T.; McIsaac, A.; Wang, L.-P.; Voorhis, T. V. What can density functional theory tell us about artificial catalytic water splitting? *Inorg. Chem.* **2014**, *53*, 6386−6397.
(57) Wu, H.; Yang, T.; Du, Y.; Shen, L.; Ho, G. W. Identification of facet-governing reactivity in hematite for oxygen evolution. *Adv. Mater.* **2018**, *30*, 1804341.
(58) Man, I. C.; Su, H.-Y.; Calle-Vallejo, F.; Hansen, H. A.; Martínez, J. I.; Inoglu, N. G.; Kitchin, J.; Jaramillo, T. F.; Nørskov, J. K.; Rossmeisl, J. Universality in oxygen evolution electrocatalysis on oxide surfaces. *ChemCatChem* **2011**, *3*, 1159−1165.

https://doi.org/10.1021/acscatal.1c01867
ACS Catal. 2021, 11, 8239−8246